J. Fluid Mech. (2003), *vol.* 481, *pp.* 149–175. © 2003 Cambridge University Press
DOI: 10.1017/S0022112003003823 Printed in the United Kingdom

Linear feedback control and estimation of transition in plane channel flow

By MARKUS HÖGBERG[1,2], THOMAS R. BEWLEY[2], AND DAN S. HENNINGSON[1,3]

[1]Department of Mechanics, Royal Institute of Technology, SE-100 44, Stockholm, Sweden

[2]Department of Mechanical and Aeronautical Engineering, University of California San Diego, La Jolla, CA 92093-0411, USA

[3]The Swedish Defence Reseach Agency (FOI), Aeronautics Division, SE-172 90 Stockholm, Sweden

(Received 25 October 2001 and in revised form 15 November 2002)

Modern linear control theory has recently been established as a viable tool for developing effective, spatially localized convolution kernels for the feedback control and estimation of linearized Navier–Stokes systems. In the present paper, the effectiveness of these kernels for significantly expanding the basin of attraction of the laminar state in a subcritical nonlinear channel flow system is quantified using direct numerical simulations for a range of Reynolds numbers ($Re_{\bar{q}} = 2000$, 3000 and 5000) and for a variety of initial conditions of physical interest. This is done by quantifying the change in the transition thresholds (see Reddy *et al.* 1998) when feedback control is applied. Such transition thresholds provide a relevant measure of performance for transition control strategies even in the nonlinear regime. Initial flow perturbations with streamwise vortices, oblique waves, and random excitations over an array of several Fourier modes are considered. It is shown that the minimum amplitude of these initial flow perturbations that is sufficient to excite nonlinear instability, and thereby promote transition to turbulence, is significantly increased by application of the control feedback. The kernels used to apply the feedback are found to decay exponentially with distance far from the origin, as predicted by the analysis of Bamieh, Paganini & Dahleh (2002). In the present paper, it is demonstrated via numerical simulation that truncation of these spatially localized convolution kernels to spatially compact kernels with finite non-zero support does not significantly degrade the effectiveness of the control feedback. In addition to the new state-feedback control results, exponential convergence of a localized physical-space state estimator with wall measurements is also demonstrated. The estimator and the full-state feedback controller are then combined to obtain a wall-information-based linear compensator. The compensator performance is also quantified, and key issues related to improving the performance of this compensator, which is degraded compared with the full-state feedback controller, are discussed.

1. Introduction

1.1. *Stability and transition in shear flows*

The process of laminar–turbulent transition is of importance in many engineering applications as well as an active research area within the field of fundamental flow physics. Laminar flows typically exhibit much less drag, mixing, and heat transfer than their turbulent counterparts, and are often more prone to separate in the presence of

https://doi.org/10.1017/S0022112003003823 Published online by Cambridge University Press

an adverse pressure gradient. Thus, effective strategies both to delay and to accelerate the transition process are of interest in a variety of engineering applications.

The transition process most often starts with the growth of small perturbations of a laminar base flow. It can therefore be modelled, at least in its initial stages, by the linearized Navier–Stokes equation. Traditionally, solutions of this equation have been characterized in terms of the exponential growth or decay rates of its individual eigenmodes. In particular, for boundary-layer and channel flows, the Fourier-transformed linearized Navier–Stokes equations may easily be manipulated into the Orr–Sommerfeld and Squire equations. The least-stable eigenmodes of this system of equations vary in the streamwise direction only, and are referred to as Tollmien–Schlichting (TS) waves. For laminar base flows without inflection points, these waves are two-dimensional and grow on a viscous time scale. In the past, the Reynolds number at which one of these waves becomes linearly unstable, the so-called critical Reynolds number, has been a feature of particular interest. The calculation of exponential growth rates and critical Reynolds numbers for a wide variety of flows has been the object of numerous efforts by researchers investigating flow stability over the last century; key results are compiled in Drazin & Reid (1981). One common path to transition is the exponential growth of two-dimensional TS-waves, followed by a secondary instability of these finite-amplitude waves to small-amplitude three-dimensional perturbations and the rapid evolution of the flow towards a fully turbulent state (see e.g. Herbert 1988).

In many shear flows, transition is observed well below the critical Reynolds number predicted by linear theory. During the last decade, several researchers have investigated the mechanisms responsible for this subcritical transition. It has been found that a key feature related to subcritical transition is the non-orthogonality of the eigenvectors of the linearized flow system, that is, the Orr–Sommerfeld/Squire operator (Butler & Farrell 1992; Reddy & Henningson 1993; Henningson & Reddy 1994). The subcritical growth in the solution to the linearized equations is associated with a superposition of non-orthogonal, decaying modes; as the individual decay rates of the superposed modes are different, destructive interference of the various modes can decrease as time evolves, leading to the possibility for transient energy growth which is sometimes quite large. Such 'non-modal growth' is often easily excited by external disturbance forces acting on the system (Trefethen *et al.* 1993). The resulting flow perturbations that grow most, which we label as 'worst-case' perturbations (but are sometimes labelled as 'optimal' perturbations, depending on the viewpoint), are perturbations which vary in the spanwise direction only, initially appearing as streamwise vortices and eventually evolving into streamwise streaks. These perturbations are fundamentally different from Tollmien–Schlichting waves, which vary in the streamwise direction only. Worst-case perturbations were, for boundary-layer and channel flows, first calculated by Butler & Farrell (1992). Several transition scenarios initiated by perturbations experiencing non-modal growth have been investigated; for a recent review of subcritical transition scenarios, see Schmid & Henningson (2001). In the present paper, we will discuss the application of modern flow control techniques to the problem of subcritical transition in plane channel flow; to set the stage, we first describe in greater detail some relevant background on the subcritical transition process.

1.2. *Canonical subcritical transition problem: plane channel flow*

Small perturbations $\{u, v, w\}$ to a laminar flow $U(y)$ in a channel (figure 1) are governed by the Orr–Sommerfeld/Squire equations. These equations are derived from the Fourier transform (in the x- and z-directions) of the Navier–Stokes equation

https://doi.org/10.1017/S0022112003003823 Published online by Cambridge University Press

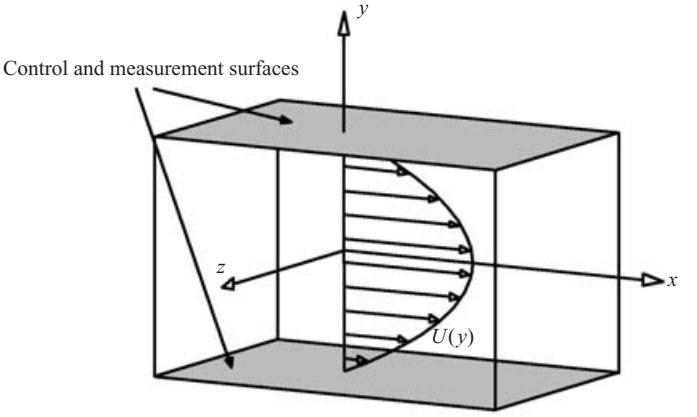


FIGURE 1. Geometry of the flow domain and coordinate system used.

linearized about a mean flow profile $U(y)$, and may be written for each wavenumber pair $\{k_x, k_z\}$ as

$$\hat{\Delta}\,\dot{\hat{v}} = \{-\mathrm{i}\,k_x\,U\,\hat{\Delta} + \mathrm{i}\,k_x\,U'' + \hat{\Delta}(\hat{\Delta}/Re_{\mathfrak{C}})\}\hat{v}, \tag{1.1a}$$

$$\dot{\hat{\omega}} = \{-\mathrm{i}\,k_z\,U'\}\;\hat{v} + \{-\mathrm{i}\,k_x\,U + \hat{\Delta}/Re_{\mathfrak{C}}\}\;\hat{\omega}, \tag{1.1b}$$

where $\hat{\omega}$ is the wall-normal vorticity, $\hat{\Delta} = \partial^2/\partial y^2 - k^2$, $k^2 = k_x^2 + k_z^2$, hats denote Fourier coefficients, and primes denote wall-normal derivatives. The Reynolds number $Re_{\mathfrak{C}} = U_{\mathfrak{C}}\,h/\nu$ parameterizes the problem, where h is the half-width of the channel, $U_{\mathfrak{C}}$ is the centreline velocity, and ν is the kinematic viscosity of the fluid. Without loss of generality, we assume the walls are located at $y = \pm 1$.

Assuming modes with exponential time dependence, the above system becomes an eigenvalue problem with two distinct solution families. The first family of solutions contains the Orr–Sommerfeld modes, which involve eigensolutions of the equation for the wall-normal velocity. The least stable Orr–Sommerfeld mode is the Tollmien–Schlichting wave mentioned earlier. For the plane channel flow problem under consideration here, there are no exponentially growing solutions for Reynolds numbers $Re_{\mathfrak{C}} < 5772$ (Orszag 1971). The second family of solutions contains the Squire modes and has zero wall-normal velocity. It can be shown that the Squire modes are always stable.

Transition experiments show that plane channel flows typically undergo transition to turbulence at Reynolds numbers as low as $Re_{\mathfrak{C}} = 1000$ (Patel & Head 1969; Carlson, Widnall & Peeters 1982). The discrepancy between the critical Reynolds number for linear instability and the Reynolds number at which transition is actually observed is a direct consequence of the non-normality of the Orr–Sommerfeld/Squire operator for the plane channel flow problem, as mentioned previously. As a result, there is a possibility of transient disturbance energy growth, which scales as $O(Re_{\mathfrak{C}}^2)$ and has a maximum magnitude of about a factor of 200 at $Re_{\mathfrak{C}} = 1000$ (Reddy & Henningson 1993). In addition, there is enhanced sensitivity of such a system to external disturbance forcing: the response of the output energy can be up to $O(Re_{\mathfrak{C}}^4)$ greater than the input disturbance energy, as explained by Trefethen *et al.* (1993). This heightened system sensitivity is mainly associated with the evolution of streamwise vortices into streamwise streaks.

https://doi.org/10.1017/S0022112003003823 Published online by Cambridge University Press

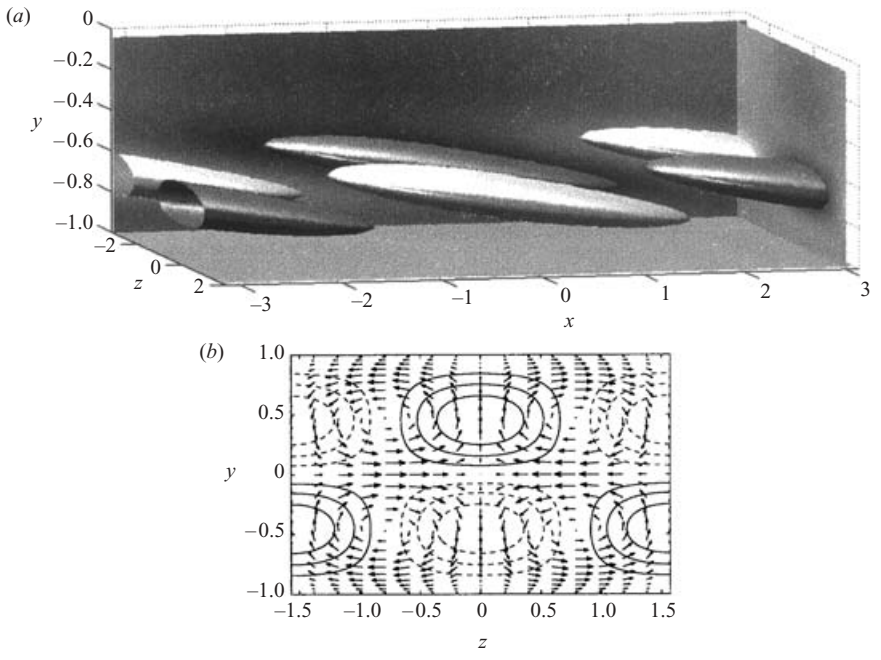


FIGURE 2. Visualizations of two of the initial flow perturbations considered in the transition threshold calculations: (*a*) oblique waves, showing positive (light) and negative (dark) isosurfaces of half of the maximum magnitude of the normal velocity, and (*b*) streamwise vortices, showing contours of v (solid contours for positive velocity and dashed for negative), and cross-flow velocity vectors (projected onto the z, y-plane) at $x = 0$.

1.3. *Characterizing nonlinear instability: transition thresholds*

Two transition scenarios starting with small initial flow perturbations experiencing large non-modal growth have been investigated by Reddy *et al.* (1998), and involve the growth of primarily spanwise-varying structures to finite amplitude followed by their subsequent secondary instability. These scenarios are initialized with (*a*) a pair of superimposed oblique waves, and (*b*) streamwise vortices with an antisymmetric v component across $y = 0$, as illustrated in figures 2(*a*) and 2(*b*). Notice that 1% random noise is added to all transition scenarios tested in order to break the symmetries. Note also that the streamwise vortices with maximum transient growth actually have a v component which is symmetric across $y = 0$; however, similar transition scenarios starting with symmetric streamwise vortices have higher threshold energies for transition (Reddy *et al.* 1998). The energy evolution in various wavenumber components of the flow for these two transition scenarios are shown in figure 3. We see in figure 3(*a*) that the oblique waves (in the $\{1, 1\}$ component) induce streamwise vortices (in the $\{0, 2\}$ and $\{0, 4\}$ components) that efficiently generate streamwise streaks (thereby undergoing relatively large transient energy growth). In figure 3(*b*) the scenario is similar, but the streamwise vortices are introduced directly (that is, as the initial flow perturbation). Secondary instability of these streamwise streaks (excited by the noise in the initial flow perturbations) ultimately causes the breakdown to turbulence.

To quantify the transition process, Reddy *et al.* (1998) defined a transition time and determined the dependence of this time on the energy of the initial flow perturbation.

https://doi.org/10.1017/S0022112003003823 Published online by Cambridge University Press

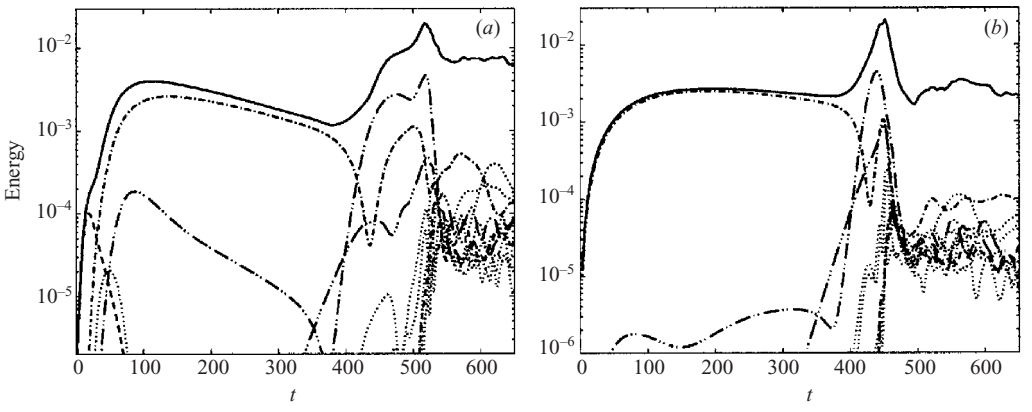


FIGURE 3. Energy evolution in various wavenumber components $\{k_x, k_z\}$ during the channel-flow transition process for (*a*) the oblique-wave transition scenario, and (*b*) the streamwise-vortex transition scenario. Plotted are: ———, the total flow perturbation energy in all wavenumber components other than $\{0, 0\}$; as well as the energy in the $\{1, 1\}$ component (– – – –), the $\{0, 2\}$ component (—·—), the $\{0, 4\}$ component (—··—), the $\{1, 2\}$ component (—···—), and the other components (·····). The Reynolds number is $Re_{\mathfrak{C}} = 2000$ and the energy density of the initial flow perturbation is 2.6×10^{-6} for the oblique wave and 1.4×10^{-5} for the streamwise vortex. Notice for comparison that the energy density of the laminar mean flow is 0.2666 in all cases.

The transition time T so defined is the time during which the friction coefficient c_f increases from its initial value (near that of the laminar flow) to half of its mean turbulent value, i.e. the time T when $c_f(T) = 0.5(c_{f,laminar} + c_{f,turbulent})$. If the turbulent state is never reached, we define T to be infinite. The lowest perturbation energy density resulting in a finite value of T is defined to be the transition threshold for that perturbation structure.

Such transition thresholds can be viewed as indicators of how sensitive the nonlinear evolution of the flow is to different initial flow perturbations, and therefore provide an excellent means of quantifying the performance of a transition control strategy on the full nonlinear system. In this paper, we will develop and test full-state feedback controllers as well as wall-information-based compensators in order to stabilize the nonlinear flow system. We will quantify the effectiveness of these control strategies in terms of how well they can increase these transition thresholds.

1.4. *Flow control background*

Using linear control theory for controlling flow instabilities is a fairly new concept. Early work on controlling instabilities in laminar flows has been mostly devoted to using the wave superposition principle for anti-phase modal suppression. The papers by Thomas (1990) and Metcalfe (1994) review the early efforts on the control of Tollmien–Schlichting (TS) waves using the anti-phase control strategy. Other reviews on flow control can be found in e.g. Gad-el-Hak (1996), Lumley & Blossey (1998), and Bewley (2001). We review here a small subset of this recent work which is related to the present paper.

Much of the focus of the flow control community in recent years has been on the problem of turbulence control and drag reduction. One of the most popular turbulence control strategies in numerical simulations is the opposition control strategy introduced by Choi, Moin & Kim (1994). With this approach, a detection

https://doi.org/10.1017/S0022112003003823 Published online by Cambridge University Press

plane for one of the velocity components is introduced in the flow near the wall (a distance from the wall of $y^+ \approx 10$ is common). The detected velocity is then phase shifted by 180° and applied as a boundary condition on the wall. With this method, the drag in a turbulent channel may be reduced by as much as 25% using the normal velocity component, and by as much as 30% using the spanwise velocity component. A similar control problem was studied by Farrell & Ioannou (1996) by applying the opposition control strategy to a linear system model. They found that the variance of their parameterized turbulence model could be reduced by as much as 70% near the wall by application of this type of strategy.

The physical mechanism behind the success of opposition control is related to manipulation of near-wall streamwise vortices. An alternative way of viewing the near-wall vortices is presented in Koumoutsakos (1999), which resulted in a control scheme providing about 40% drag reduction in a turbulent channel flow at $Re_\tau = 180$. This feedback control scheme relies on measurement and control of the spanwise 'vorticity flux' at the wall. Lee *et al.* (1997) used a neural network to find adaptively a feedback law for the local wall shear stress, achieving about 20% drag reduction. This paper also approximated the converged neural network rule by a simple linear control rule; this simpler strategy was found to have almost the same effectiveness on the turbulent flow.

Possible applications in fluid mechanics of gradient-based 'optimal' control techniques were identified and analysed in the seminal paper by Abergel & Temam (1990). These techniques optimize the evolution of a partial differential equation system over a finite time horizon with gradient-based strategies derived from the calculation of an appropriately defined adjoint field. Choi *et al.* (1993) introduced the so-called 'suboptimal' approximation of the optimal control problem. This approximation significantly simplifies the numerical computations required to compute the control in such an algorithm by, among other approximations, considering only an infinitesimal time horizon each time the control is computed. By so doing, difficult nonlinear terms may be approximated or neglected, effectively introducing a 'Stokes model' for determining the controls for a Navier–Stokes system. This methodology was applied to a turbulent channel flow at $Re_\tau = 100$ by Bewley & Moin (1994), resulting in a 17% drag reduction. The related suboptimal control work of Lee, Kim & Choi (1998) also uses the suboptimal approximation to derive appropriate control strategies targeting carefully designed objective functions based on wall pressure fluctuations or wall shear stress. This work resulted in a skin friction drag reduction of up to 22%.

When the 'suboptimal' approximation is not used, optimization of controls in the cumbersome receding-horizon model-predictive control (MPC) setting is required. With such a strategy, the evolution of the system over a finite time interval is considered, and the controls are optimized over this finite interval using an iterative, gradient-based strategy. Once optimized, the controls over a subset of this finite time interval are applied to the evolving flow system, then the iterative optimization procedure is begun anew on a new time interval. It is possible with this method to completely relaminarize the flow in a channel with turbulent initial conditions at $Re_\tau = 100$, and this has been done using direct numerical simulations (DNS) by Bewley, Moin & Temam (2001) and in related work using large-eddy simulations (LES) by Collis *et al.* (2000).

In many applications, it seems plausible that transition to turbulence can be substantially delayed by application of linear control feedback. By so doing, the need for turbulence control strategies which are effective in the nonlinear regime can be avoided. Since energy growth in a fluid flow is a linear process, linear-model-based

https://doi.org/10.1017/S0022112003003823 Published online by Cambridge University Press

control strategies based on the linearized equations of fluid motion are appropriate for at least the linear stages of the transition process. Based on the findings reported by e.g. Henningson (1996); Farrell & Ioannou (1996) and Kim & Lim (2000), the importance of linear mechanisms for sustaining turbulence, especially the coupling between normal velocity and normal vorticity, indicate that linear controllers might also be useful in controlling fully developed turbulence. Use of the linearized equations for flow control was considered in Hu & Bau (1994), where a simple proportional control strategy based on wall shear measurements was used to stabilize a laminar plane channel flow through heating and cooling of the walls in order to change the viscosity of the flow. This work suggested that the influence of the applied control on the domain of attraction of the laminar state should be quantified. This is similar to what is accomplished in the present work using model-based control algorithms. In the paper by Joshi, Speyer & Kim (1997), classical linear control theory was applied to stabilize the flow in a two-dimensional channel using blowing and suction on the channel walls coordinated with measurements of the wall shear. The control problem was formulated using a streamfunction approach suitable for two-dimensional problems. Extension of this work using modern control theory and employing model reduction for the compensator is presented in Joshi, Speyer & Kim (1999), and the corresponding multi-wavenumber case is treated in Cortelezzi *et al.* (1998). In Lee *et al.* (2001) extension of the two-dimensional controller to a three-dimensional one by augmenting an *ad hoc* scheme in the third direction is suggested and tested in a turbulent flow. The streamfunction formulation was also used by Baramov *et al.* (2000) to apply robust ($\mathscr{H}_\infty$) control to the two-dimensional fluid system with multi-wavenumber control, accounting for effects of localized actuation and sensing. A complete formulation for model-based control of three-dimensional perturbations is presented in Bewley & Liu (1998).

The present paper builds on the work by Bewley & Liu (1998), where both optimal ($\mathscr{H}_2$) and robust ($\mathscr{H}_\infty$) control strategies were applied to isolated wavenumber pairs in a linearized channel flow system with three-dimensional perturbations. The $\mathscr{H}_2$ problem was extended, using a slightly modified formulation, to compute the feedback gains for a large array wavenumber pairs in Högberg & Bewley (2000). Upon inverse Fourier transform, a control law was found in which the control gains, which are now expressed as convolution kernels, are localized in physical space (that is, they eventually decay exponentially in space away from the origin) and are resolved well on the numerical grid. These control kernels were found to be independent of both the grid resolution and the size of the computational box, so long as the grid was sufficiently fine and the box size sufficiently large. Application of these linear controllers to instabilities in spatial boundary layer flows was performed in Högberg & Henningson (2002) for stationary as well as time-varying perturbations in Blasius and Falkner–Skan–Cooke boundary layers.

1.5. *Outline of the paper*

In the current paper, the ability of constant-gain linear controllers to prevent transition in channel flows is investigated and quantified. Transition thresholds are used as a relevant measure of performance, allowing quantitative comparisons of different control schemes in terms of how well they work to inhibit transition to turbulence in the full nonlinear channel flow system. We also introduce a state estimator, in the form of an extended Kalman filter, that can be used to reconstruct the flow field from wall measurements with exponential convergence. This problem is 'dual' to the state-feedback control problem, meaning that the solution technique is closely related

https://doi.org/10.1017/S0022112003003823 Published online by Cambridge University Press

to the solution technique used for solving the state-feedback control problem. The state estimator is then combined with the controller, and the ability of the resulting compensator to prevent transition in channel flow based on wall information only is quantified using similar techniques.

The remainder of this paper is organized as follows. In § 2, the governing equations and the formulation of the control and estimation problem is reviewed. Properties of the resulting control and estimation kernels are discussed and a short description of the numerical methods used is given. In § 3, the results of the many simulations required to determine the transition thresholds are summarized for both the full-state feedback case and the wall-information-based compensator case which combines the state-feedback controller with an extended Kalman filter. Conclusions are outlined in § 4.

2. Approach

The initial stages of transition are accurately modeled by the linearized Navier–Stokes equations. Straightforward manipulation of these equations results in the Orr–Sommerfeld/Squire equations for small perturbations to a mean flow. These equations can be transformed into Fourier space, where the equations for different wavenumber pairs completely decouple and can be treated separately (equations (1.1*a*) and (1.1*b*)). Bewley & Liu (1998) suggested computing optimal control and estimator feedback rules for each wavenumber pair separately in Fourier space, and then combining them in an inverse Fourier transform, resulting in physical-space convolution kernels describing the control and estimation feedback rules. The elegant analysis of Bamieh, Paganini & Dahleh (2002) (also reported in Bamieh, Paganini & Dahleh 1998, 1999; Paganini & Bamieh 1998) proved that, for a broad class of spatially invariant systems such as the present one, the corresponding control and estimation convolution kernels will be 'spatially localized', meaning that they will decay exponentially in space sufficiently far from the origin. Truncation of such localized kernels results in kernels with spatially compact non-zero support (that is, the truncated kernels are zero outside a finite radius of the origin). Since the localized kernels eventually decay exponentially, this truncation may be performed to any desired degree of accuracy. It is found that the shape of the truncated kernels so computed converges as the box size is increased; this effectively relaxes the artificial assumption of spatial periodicity imposed by utilizing the Fourier series representation in the kernel derivation. In practice, this enables the convolution kernels so computed to be used in a periodic channel of any size, or, in fact, in the physical case of non-spatially periodic flows (i.e. in the limit of a spatially periodic box of infinite length and width). In § 2.3.2, it is demonstrated that the current approach indeed yields such localized kernels with exponential decay. The issue of controlling and estimating infinite-dimensional systems based on a finite-dimensional models is discussed further in e.g. Ito & Morris (1998), where details of the mathematical properties of the Riccati equations are also presented.

2.1. *Summary of the derivation of the linear compensator*

In this section, we give a brief summary of the derivation of the control and estimation problem. As a first step, the governing equations need to be put in a form suitable for application of standard control theory. The Orr–Sommerfeld/Squire equations (1.1*a*) and (1.1*b*) are usually written with a Laplacian operator on the left-hand side. Fortunately, this Laplacian operator can, with care, be inverted if the boundary

https://doi.org/10.1017/S0022112003003823 Published online by Cambridge University Press

conditions are taken into account properly, thus resulting in the desired form of the governing equations:

$$\dot{\hat{v}} = \underbrace{\hat{\Delta}^{-1}\{-\mathrm{i}k_x U\,\hat{\Delta} + \mathrm{i}k_x U'' + \hat{\Delta}(\hat{\Delta}/Re_{\tau})\}}_{\hat{L}_{OS}}\,\hat{v}, \tag{2.1a}$$

$$\dot{\hat{\omega}} = \underbrace{\{-\mathrm{i}k_z U'\}}_{\hat{L}_C}\,\hat{v} + \underbrace{\{-\mathrm{i}k_x U + \hat{\Delta}/Re_{\tau}\}}_{\hat{L}_{SQ}}\,\hat{\omega}. \tag{2.1b}$$

Writing these equations in operator form, we obtain

$$\dot{\hat{\boldsymbol{x}}} = \boldsymbol{N}\hat{\boldsymbol{x}}, \tag{2.2}$$

where

$$\boldsymbol{N} = \begin{pmatrix} \hat{L}_{OS} & 0 \\ \hat{L}_C & \hat{L}_{SQ} \end{pmatrix} \quad \text{and} \quad \hat{\boldsymbol{x}} = \begin{pmatrix} \hat{v} \\ \hat{\omega} \end{pmatrix}.$$

The control ϕ is the wall-normal velocity component at the walls: $\hat{\boldsymbol{\phi}} = \begin{pmatrix} \hat{v}(+1) \\ \hat{v}(-1) \end{pmatrix}$.

In order to formulate an appropriate objective function, we will make use of the expression for the energy E of the flow perturbations:

$$E = \frac{1}{2V}\int_{\Omega}(u^2+v^2+w^2)\,\mathrm{d}V = \sum_{k_x,k_z}\frac{1}{8k^2}\int_{-1}^{1}\left(k^2|\hat{v}|^2 + \left|\frac{\partial\hat{v}}{\partial y}\right|^2 + |\hat{\omega}|^2\right)\mathrm{d}y$$

$$= \sum_{k_x,k_z}\boldsymbol{E}(k_x,k_z). \tag{2.3}$$

Note that we have defined $\boldsymbol{E}(k_x,k_z)$ as the contribution of the component of the flow perturbation at each $\{k_x,k_z\}$ wavenumber to the total energy E; by Parseval's theorem, these contributions are completely decoupled. In the present notation, these contributions may be written as $\boldsymbol{E} = \hat{\boldsymbol{x}}^*\boldsymbol{Q}\hat{\boldsymbol{x}}$, where the operator $\boldsymbol{Q}$ is made up of the several operators needed to describe the energy measure, as illustrated above, and the asterisk denotes the conjugate transpose. Due to the separation principle of optimal control theory, implying that the dynamics of the controlled state and the closed-loop estimation error are decoupled (see e.g. Skelton 1988, p. 411), the estimation and control problems may be treated separately in the derivation that follows.

2.1.1. *Control strategy*

In order to obtain a standard state-space representation of the boundary-controlled Orr–Sommerfeld/Squire equations, to which standard linear control theory may be applied, the inhomogeneous boundary condition forcing needs to be accounted for properly. By a straightforward 'lifting' procedure, the effect of the boundary condition forcing on the original flow system can be represented by volume forcing near the wall in a modified system with homogeneous boundary conditions. Using the principle of superposition, the solution of the original system with inhomogeneous boundary conditions, $\hat{\boldsymbol{x}}$, can be recovered by combining this 'homogeneous solution', $\hat{\boldsymbol{x}}_h$, with an appropriately defined 'particular solution', $\hat{\boldsymbol{x}}_p$, which is used simply to relate the boundary conditions to the volume forcing in a convenient manner; that is

$$\hat{\boldsymbol{x}} = \hat{\boldsymbol{x}}_h + \hat{\boldsymbol{x}}_p \rightarrow \begin{cases} \hat{v} = \hat{v}_h + \hat{v}_p, \\ \hat{\omega} = \hat{\omega}_h + \hat{\omega}_p. \end{cases} \tag{2.4}$$

https://doi.org/10.1017/S0022112003003823 Published online by Cambridge University Press

In the present system, two particular solutions are used for each wavenumber pair $\{k_x, k_z\}$, one to account for the lifting of the control applied at the top wall, and the other to account for the lifting of the control applied at the bottom wall; these particular solutions are denoted by $\hat{\boldsymbol{x}}_p = \boldsymbol{Z}\hat{\boldsymbol{\phi}}$ (note that $\hat{\boldsymbol{\phi}}$ has two components, one for each wall). Using the subscript s to indicate the fact that we have finally arrived at the 'standard state-space form', the resulting system of equations for each wavenumber pair $\{k_x, k_z\}$ may now be written as

$$\dot{\hat{\boldsymbol{x}}}_s = \boldsymbol{A}\hat{\boldsymbol{x}}_s + \boldsymbol{B}\hat{\boldsymbol{u}}_s,$$

where

$$\boldsymbol{A} = \begin{pmatrix} \boldsymbol{N} & \boldsymbol{NZ} \\ 0 & 0 \end{pmatrix}, \quad \boldsymbol{B} = \begin{pmatrix} -\boldsymbol{Z} \\ \boldsymbol{I} \end{pmatrix}, \quad \hat{\boldsymbol{x}}_s = \begin{pmatrix} \hat{\boldsymbol{x}}_h \\ \hat{\boldsymbol{\phi}} \end{pmatrix}, \quad \hat{\boldsymbol{u}}_s = \frac{\partial \hat{\boldsymbol{\phi}}}{\partial t}.$$

Note that the control variable in this formulation of the system is actually the *time derivative* of the normal velocity on the walls. This formulation for the state equation, in addition to being the natural outcome of the lifting procedure, allows us to penalize the time derivative of the blowing/suction distribution directly in the cost function, thus resulting in a control strategy which generates 'regular' (that is, smoothly varying) control distributions on the wall. In the present work, the particular solutions are defined such that $\boldsymbol{N}\hat{\boldsymbol{x}}_p = 0$, which simplifies the resulting equations significantly. The energy measure may now be written

$$\boldsymbol{E} = \hat{\boldsymbol{x}}_s^* \begin{pmatrix} \boldsymbol{Q} & \boldsymbol{QZ} \\ \boldsymbol{Z}^*\boldsymbol{Q} & \boldsymbol{Z}^*\boldsymbol{QZ} \end{pmatrix} \hat{\boldsymbol{x}}_s = \hat{\boldsymbol{x}}_s^* \hat{\boldsymbol{Q}}_s \hat{\boldsymbol{x}}_s.$$

Defining an objective function combining measures of the flow perturbation energy and the 'control effort',

$$\hat{J} = \int_0^\infty (\hat{\boldsymbol{x}}_s^* \hat{\boldsymbol{Q}}_s \hat{\boldsymbol{x}}_s + \ell^2 \hat{\boldsymbol{u}}_s^* \hat{\boldsymbol{u}}_s)\, \mathrm{d}t,$$

the control $\hat{\boldsymbol{u}}_s$ minimizing $\hat{J}$ may now be found with standard control theory:

$$\hat{\boldsymbol{u}}_s = \hat{\boldsymbol{K}}_s \hat{\boldsymbol{x}}_s, \quad \text{where} \quad \hat{\boldsymbol{K}}_s = -\frac{1}{\ell^2}\boldsymbol{B}^*\boldsymbol{X}$$

and $\boldsymbol{X}$ is the Hermetian positive-definite solution to the operator Riccati equation

$$\left(\boldsymbol{AX} + \boldsymbol{XA}^* - \boldsymbol{XB}\frac{1}{\ell^2}\boldsymbol{B}^*\boldsymbol{X} + \hat{\boldsymbol{Q}}_s\right)\hat{\boldsymbol{x}}_s = 0 \quad \forall \text{ admissible } \hat{\boldsymbol{x}}_s. \tag{2.5}$$

Notice that ℓ^2 is an adjustable parameter regulating a penalty on the integral of the square of the *time derivative* of the blowing/suction distribution on the walls, allowing the control design to impose a degree of 'regularity' on the control distribution. The integral of the square of the control velocity itself is naturally penalized through the lifting terms in $\hat{\boldsymbol{Q}}_s$; though additional control penalties on this term could be imposed, this was not found to be necessary in the present work. Due to the specific definition of $\hat{\boldsymbol{x}}_s$ used above, the feedback rule $\hat{\boldsymbol{K}}_s(k_x, k_z)$ so obtained is for feedback of the homogeneous part of the flow only. By modifying $\hat{\boldsymbol{K}}_s(k_x, k_z)$ to incorporate the effect of the feedback of the inhomogeneous part of the flow, kernels for the total flow

https://doi.org/10.1017/S0022112003003823 Published online by Cambridge University Press

may now be obtained. Decomposing $\hat{\boldsymbol{u}}_s = \hat{\boldsymbol{K}}_s \hat{\boldsymbol{x}}_s$ and $\hat{\boldsymbol{x}}_p = \boldsymbol{Z}\hat{\boldsymbol{\phi}}$ according to

$$\begin{pmatrix} \dot{\hat{v}}(+1) \\ \dot{\hat{v}}(-1) \end{pmatrix} = \begin{pmatrix} \hat{\boldsymbol{K}}_{s,+1,\hat{v}_h} & \hat{\boldsymbol{K}}_{s,+1,\hat{\omega}_h} & \hat{\boldsymbol{K}}_{s,+1,\hat{v}(+1)} & \hat{\boldsymbol{K}}_{s,+1,\hat{v}(-1)} \\ \hat{\boldsymbol{K}}_{s,-1,\hat{v}_h} & \hat{\boldsymbol{K}}_{s,-1,\hat{\omega}_h} & \hat{\boldsymbol{K}}_{s,-1,\hat{v}(+1)} & \hat{\boldsymbol{K}}_{s,-1,\hat{v}(-1)} \end{pmatrix} \begin{pmatrix} \hat{v}_h \\ \hat{\omega}_h \\ \hat{v}(+1) \\ \hat{v}(-1) \end{pmatrix},$$

$$\begin{pmatrix} \hat{v}_p \\ \hat{\omega}_p \end{pmatrix} = \begin{pmatrix} \boldsymbol{Z}_{\hat{v}_p,\hat{v}(+1)} & \boldsymbol{Z}_{\hat{v}_p,\hat{v}(-1)} \\ \boldsymbol{Z}_{\hat{\omega}_p,\hat{v}(+1)} & \boldsymbol{Z}_{\hat{\omega}_p,\hat{v}(-1)} \end{pmatrix} \begin{pmatrix} \hat{v}(+1) \\ \hat{v}(-1) \end{pmatrix},$$

it is convenient to rearrange the gain matrix $\hat{\boldsymbol{K}}_s$ into a form $\hat{\boldsymbol{K}}$ with which the simple control feedback rule $\hat{\boldsymbol{u}}_s = \hat{\boldsymbol{K}}\hat{\boldsymbol{x}}$ may be employed. Decomposing this new feedback rule such that

$$\begin{pmatrix} \dot{\hat{v}}(+1) \\ \dot{\hat{v}}(-1) \end{pmatrix} = \begin{pmatrix} \hat{\boldsymbol{K}}_{+1,\hat{v}} & \hat{\boldsymbol{K}}_{+1,\hat{\omega}} \\ \hat{\boldsymbol{K}}_{-1,\hat{v}} & \hat{\boldsymbol{K}}_{-1,\hat{\omega}} \end{pmatrix} \begin{pmatrix} \hat{v} \\ \hat{\omega} \end{pmatrix} \tag{2.6}$$

and defining

$$\hat{\boldsymbol{K}}_{\pm1,\hat{v}(+1)} = \hat{\boldsymbol{K}}_{s,\pm1,\hat{v}(+1)} - \hat{\boldsymbol{K}}_{s,\pm1,\hat{v}_h}\boldsymbol{Z}_{\hat{v}_p,\hat{v}(+1)} - \hat{\boldsymbol{K}}_{s,\pm1,\hat{\omega}_h}\boldsymbol{Z}_{\hat{\omega}_p,\hat{v}(+1)}$$
$$\hat{\boldsymbol{K}}_{\pm1,\hat{v}(-1)} = \hat{\boldsymbol{K}}_{s,\pm1,\hat{v}(-1)} - \hat{\boldsymbol{K}}_{s,\pm1,\hat{v}_h}\boldsymbol{Z}_{\hat{v}_p,\hat{v}(-1)} - \hat{\boldsymbol{K}}_{s,\pm1,\hat{\omega}_h}\boldsymbol{Z}_{\hat{\omega}_p,\hat{v}(-1)},$$

it follows that

$$\hat{\boldsymbol{K}}_{\pm1,\hat{v}} = \begin{pmatrix} \hat{\boldsymbol{K}}_{\pm1,\hat{v}(+1)} & \hat{\boldsymbol{K}}_{s,\pm1,\hat{v}_h} & \hat{\boldsymbol{K}}_{\pm1,\hat{v}(-1)} \end{pmatrix}$$
$$\hat{\boldsymbol{K}}_{\pm1,\hat{\omega}} = \begin{pmatrix} 0 & \hat{\boldsymbol{K}}_{s,\pm1,\hat{\omega}_h} & 0 \end{pmatrix}.$$

The feedback control rule $\hat{\boldsymbol{u}}_s = \hat{\boldsymbol{K}}\hat{\boldsymbol{x}}$ effectively performs a discrete integration in y across the channel, with the gains $\hat{\boldsymbol{K}}_{\pm1,\hat{v}}$ and $\hat{\boldsymbol{K}}_{\pm1,\hat{\omega}}$ as weights. As a cosine stretching function is used for the distribution of gridpoints in the y-direction in this formulation (see Bewley & Liu 1998), it is necessary to scale the control gains appropriately in order to convert the gain $\hat{\boldsymbol{K}}$ in (2.6) to a grid-independent weighting function $\hat{\boldsymbol{K}}$ on a continuous integral of the form

$$\dot{\hat{v}}(y = \pm1) = \int_{-1}^{1} [\hat{\boldsymbol{K}}_{\pm1,\hat{v}}(\bar{y})\hat{v}(\bar{y}) + \hat{\boldsymbol{K}}_{\pm1,\hat{\omega}}(\bar{y})\hat{\omega}(\bar{y})]\mathrm{d}\bar{y} \tag{2.7}$$

at each wavenumber pair $\{k_x, k_z\}$. We denote the necessary (and straightforward) transformation symbolically as $\hat{\boldsymbol{K}} = \boldsymbol{\Xi}^{-1}\hat{\boldsymbol{K}}$. Incorporation of the weights $\hat{\boldsymbol{K}}$ into a nonlinear DNS code, in turn, requires scaling of the control gains by the grid stretching function used in the nonlinear simulation code in a similar fashion. Feedback rules are computed for an array of wavenumber pairs and then inverse Fourier transformed to physical space to give the feedback law as a convolution integral of the form,

$$\dot{v}(x, y = \pm1, z, t) = \int_{\Omega} (K_{\pm1,v}(x - \bar{x}, \bar{y}, z - \bar{z})v(\bar{x}, \bar{y}, \bar{z}, t) + K_{\pm1,\omega}(x - \bar{x}, \bar{y}, z - \bar{z})\omega(\bar{x}, \bar{y}, \bar{z}, t))\,\mathrm{d}\bar{x}\,\mathrm{d}\bar{y}\,\mathrm{d}\bar{z}, \tag{2.8}$$

where $K_{\pm1,v}$ and $K_{\pm1,\omega}$ denote the physical-space feedback convolution kernels relating $\dot{v}$ at the upper and lower walls to the wall-normal velocity and wall-normal vorticity, respectively, inside the flow domain. Typical control kernels are shown in figure 4. For kernels computed via a similar procedure for the Falkner–Skan–Cooke boundary layer profiles, see Högberg & Henningson (2002).

https://doi.org/10.1017/S0022112003003823 Published online by Cambridge University Press

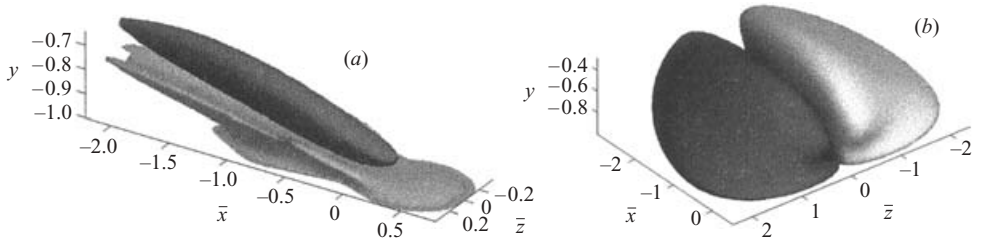


FIGURE 4. Localized controller gains relating the state $\boldsymbol{x}$ inside the domain to the control forcing $\boldsymbol{u}$ at the point $\{x = 0, y = -1, z = 0\}$ on the wall: visualized are a positive (light) and negative (dark) isosurface of the convolution kernels for (*a*) the wall-normal component of velocity and (*b*) the wall-normal component of vorticity, plotting isovalues of ± 200 and ± 1 respectively. With the present choice of the non-dimensionalization, the peak magnitude of the kernel in (*a*) is 3300 and the peak magnitude of the kernel in (*b*) is 17.5; to facilitate comparison, the isosurface values are chosen at $\sim 6\%$ of the peak value in both plots. The kernels were computed with $\ell = 1$ and $Re_{\mathfrak{C}} = 2000$, and the distances indicated are normalized such that the channel half-width is unity.

2.1.2. *Estimator strategy*

Estimating the state of the flow based on measurements at the wall is a 'dual' problem to that of controlling the flow with wall actuation, in the sense that a closely related mathematical procedure is used. In this problem, a computational model for an 'estimate' of the current state of the flow system is first written down. (In a physical implementation, this equation for the state estimate is computed in real time inside the controlling electronics as the flow system evolves.) An equation for the error of the state estimate is then determined, and volume forcing on the computational model is sought to minimize some measure of the estimation error. An estimator of this type is known as a Kalman filter, and is a standard problem. The single wavenumber case was considered in Bewley & Liu (1998) with a problem formulation similar to the one used in the present paper. Following the work done there, we now model the state equation (2.2) and the skin-friction measurements of our system as disturbed by a random (zero-mean white Gaussian) process $\hat{\boldsymbol{w}}$ such that

$$\dot{\hat{\boldsymbol{x}}}_h = \boldsymbol{N}\hat{\boldsymbol{x}}_h + \boldsymbol{B}_1\hat{\boldsymbol{w}} - \boldsymbol{Z}\dot{\hat{\boldsymbol{\phi}}} \tag{2.9}$$

$$\hat{\boldsymbol{y}}_h = \boldsymbol{C}_2\hat{\boldsymbol{x}}_h + \boldsymbol{D}_{21}\hat{\boldsymbol{w}}, \tag{2.10}$$

where

$$\boldsymbol{B}_1 = (\boldsymbol{G}_1 \quad 0), \qquad \boldsymbol{C}_2\hat{\boldsymbol{x}}_h = \frac{\boldsymbol{G}_2^{-1}}{Re_{\mathfrak{C}}} \begin{pmatrix} \left.\dfrac{\partial \hat{\omega}_h}{\partial y}\right|_{y=+1} \\ \left.\dfrac{\partial \hat{\omega}_h}{\partial y}\right|_{y=-1} \end{pmatrix}, \qquad \boldsymbol{D}_{21} = (0 \quad \alpha \boldsymbol{I}),$$

where $\boldsymbol{G}_1$ is defined as the square root of the expected covariance of the state disturbances and $\alpha \boldsymbol{G}_2$ is defined as the square root of the expected covariance of the measurement noise. We assume that these covariances are time invariant and that the covariance of the measurement noise is non-singular. The problem is scaled such that $\bar{\sigma}(\boldsymbol{G}_1^2) = 1$, and α is selected such that $\bar{\sigma}(\boldsymbol{G}_2^2) = 1$. Any known structure of the disturbance covariances entering the problem should thus be accounted for in the selection of the characteristics of $\boldsymbol{G}_1$ and $\boldsymbol{G}_2$ (both with unity maximum singular value) during the compensator design, retaining the quantity α to reflect the balance

https://doi.org/10.1017/S0022112003003823 Published online by Cambridge University Press

between the magnitude of the measurement noise and the magnitude of the state disturbances. Given that the blowing/suction distribution $\hat{\boldsymbol{\phi}}$ and the lifting function $\boldsymbol{Z}$ are known, the (noisy) measurements $\hat{\boldsymbol{y}}_h$ of the quantity $\boldsymbol{C}_2\hat{\boldsymbol{x}}_h$ may be extracted easily from the available (noisy) wall measurements of the streamwise or spanwise drag. Only the field $\hat{\boldsymbol{x}}_h$ needs to be estimated in order to construct an estimate of the complete state vector $\hat{\boldsymbol{x}}_s$ (or, indeed, to estimate $\hat{\boldsymbol{x}}$ itself); we will denote our estimate of $\hat{\boldsymbol{x}}_h$ as $\hat{\boldsymbol{x}}_e$, and our estimate of $\hat{\boldsymbol{y}}_h$ as $\hat{\boldsymbol{y}}_e$. The model of the system which we will use in our estimator is

$$\left.\begin{aligned} \dot{\hat{\boldsymbol{x}}}_e &= \boldsymbol{N}\hat{\boldsymbol{x}}_e - \boldsymbol{Z}\dot{\hat{\boldsymbol{\phi}}} - \hat{\boldsymbol{\psi}}, \\ \hat{\boldsymbol{y}}_e &= \boldsymbol{C}_2\hat{\boldsymbol{x}}_e, \\ \hat{\boldsymbol{\psi}} &= \hat{\boldsymbol{L}}\Delta\hat{\boldsymbol{y}} = \hat{\boldsymbol{L}}(\hat{\boldsymbol{y}}_h - \hat{\boldsymbol{y}}_e). \end{aligned}\right\} \tag{2.11}$$

Note that the (unknown) effects of the disturbances $\hat{\boldsymbol{w}}$ are not included in the estimator model. The estimator feedback rule $\hat{\boldsymbol{\psi}} = \hat{\boldsymbol{L}}\Delta\hat{\boldsymbol{y}}$ minimizing the expected value of the L^2-norm of the estimation error is given by

$$\hat{\boldsymbol{L}} = -\frac{1}{\alpha^2}\boldsymbol{Y}\boldsymbol{C}_2^*,$$

where $\boldsymbol{Y}$ is the Hermetian positive-definite solution to the operator Riccati equation

$$\left(\boldsymbol{N}^*\boldsymbol{Y} + \boldsymbol{Y}\boldsymbol{N} - \boldsymbol{Y}\boldsymbol{C}_2^*\frac{1}{\alpha^2}\boldsymbol{C}_2\boldsymbol{Y} + \boldsymbol{B}_1\boldsymbol{B}_1^*\right)\hat{\boldsymbol{x}}_e = 0 \quad \forall \text{ admissible } \hat{\boldsymbol{x}}_e, \tag{2.12}$$

in accordance with standard Kalman filter theory. Note that α^2, which models the assumed quality of the measurements, is used as an adjustable parameter to scale the estimator feedback. Note also that the estimator feedback rule $\hat{\boldsymbol{\psi}} = \hat{\boldsymbol{L}}\Delta\hat{\boldsymbol{y}}$ decomposes according to

$$\begin{pmatrix} \hat{\boldsymbol{\psi}}_{\hat{v}_e} \\ \hat{\boldsymbol{\psi}}_{\hat{\omega}_e} \end{pmatrix} = \begin{pmatrix} \hat{\boldsymbol{L}}_{\hat{v}_e,+1} & \hat{\boldsymbol{L}}_{\hat{v}_e,-1} \\ \hat{\boldsymbol{L}}_{\hat{\omega}_e,+1} & \hat{\boldsymbol{L}}_{\hat{\omega}_e,-1} \end{pmatrix} \begin{pmatrix} \Delta\hat{y}(+1) \\ \Delta\hat{y}(-1) \end{pmatrix}.$$

Unlike the control feedback $\hat{\boldsymbol{K}}$, the estimator feedback $\hat{\boldsymbol{L}}$ represents the estimator model forcing per unit length in the y-direction. Thus, simple interpolation of the discrete quantity $\hat{\boldsymbol{L}}$ is sufficient to determine a continuous weighting function $\hat{L}$ by which a continuous analogue of the discrete estimator (2.11) may be forced via feedback of the form

$$\left.\begin{aligned} \hat{\psi}_{\hat{v}_e}(y) &= \hat{L}_{\hat{v}_e,+1}(y)\Delta\hat{y}(+1) + \hat{L}_{\hat{v}_e,-1}(y)\Delta\hat{y}(-1)], \\ \hat{\psi}_{\hat{\omega}_e}(y) &= \hat{L}_{\hat{\omega}_e,+1}(y)\Delta\hat{y}(+1) + \hat{L}_{\hat{\omega}_e,-1}(y)\Delta\hat{y}(-1)]. \end{aligned}\right\}, \tag{2.13}$$

The Kalman filter problem described above has been derived for each wavenumber pair $\{k_x, k_z\}$ independently. The inverse Fourier transform of the Fourier-space estimator feedback rule is given by the following convolution sums in physical space:

$$\begin{aligned} \psi_{v_e}(x,y,z,t) = \int \big(&L_{v_e,+1}(x-\bar{x},y,z-\bar{z})\,\Delta y(\bar{x},+1,\bar{z},t) \\ &+ L_{v_e,-1}(x-\bar{x},y,z-\bar{z})\,\Delta y(\bar{x},-1,\bar{z},t)\big)\,\mathrm{d}\bar{x}\,\mathrm{d}\bar{z}, \\ \psi_{\omega_e}(x,y,z,t) = \int \big(&L_{\omega_e,+1}(x-\bar{x},y,z-\bar{z})\,\Delta y(\bar{x},+1,\bar{z},t) \\ &+ L_{\omega_e,-1}(x-\bar{x},y,z-\bar{z})\,\Delta y(\bar{x},-1,\bar{z},t)\big)\,\mathrm{d}\bar{x}\,\mathrm{d}\bar{z}, \end{aligned}$$

https://doi.org/10.1017/S0022112003003823 Published online by Cambridge University Press

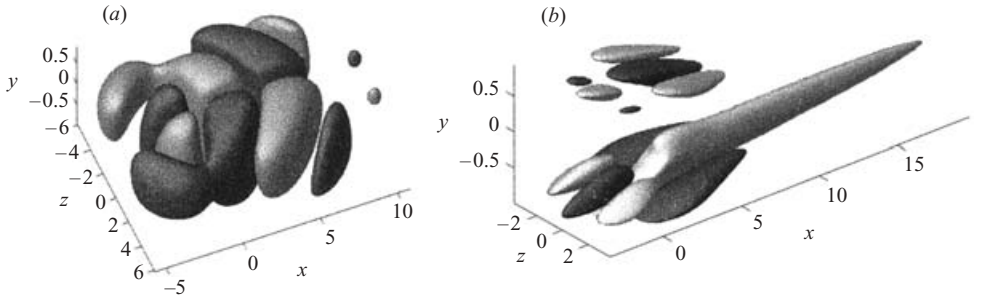


FIGURE 5. Localized estimator gains relating the measurement error $(\boldsymbol{y} - \hat{\boldsymbol{y}})$ at the point $\{x = 0, y = -1, z = 0\}$ on the wall to the estimator forcing terms $\boldsymbol{v}$ inside the domain: visualized are a positive (light) and negative (dark) isosurfaces of the convolution kernels for (*a*) the wall-normal component of velocity and (*b*) the wall-normal component of vorticity, plotting isovalues of ± 0.001 and ± 0.035 respectively. With the present choice of the non-dimensionalization, the peak magnitude of the kernel in (*a*) is 0.014 and the peak magnitude of the kernel in (*b*) is 0.58, as in figure 4, to facilitate comparison, the isosurface values are chosen at $\sim 6\%$ of the peak value in both plots. The kernels were computed with $\alpha = 100$ and $Re_{\mathfrak{L}} = 2000$.

where the estimator forcing kernels $L_{v_e,\pm 1}(x, y, z)$ and $L_{\omega_e,\pm 1}(x, y, z)$ are the inverse Fourier transforms of $\hat{L}_{\hat{v}_e,\pm 1}(k_x, y, k_z)$ and $\hat{L}_{\hat{\omega}_e,\pm 1}(k_x, y, k_z)$ respectively. The structure of L represents the forcing of the model equation in the estimator as a function of a measurement error at a single point. Using $\Delta y(\bar{x}, -1, \bar{z}) = \Delta y_o \delta(\bar{x})\delta(\bar{z})$ in the convolution integral results in $\psi_{v_e}(x, y, z) = L_{v_e,-1}(x, y, z)\Delta y_o$ and $\psi_{\omega_e}(x, y, z) = L_{\omega_e,-1}(x, y, z)\Delta y_o$, which facilitates this interpretation. Typical estimator forcing kernels are shown in figure 5.

2.2. *Computation of linear feedback kernels*

To obtain the numerical results reported in the sections that follow, control and estimator feedback gains were computed for a large array of wavenumber pairs and then inverse-transformed to physical space, as described above. The Orr–Sommerfeld/Squire system was discretized in the wall-normal direction using Chebyshev collocation such that

$$f_i = f(y_i), \quad y_i = \cos\frac{\mathrm{i}\pi}{N}, \quad i = 0, 1, \ldots, N.$$

As reported in the sections that follow, we took $N \approx 100$ in this work. The Differentiation Matrix Suite by Weideman & Reddy (2000) was used to create the differentiation matrices by which the matrix operators for the state equation were computed. Since a lifting technique is used in the present formulation (see § 2.1.1), the matrices for the homogeneous system can be found using the clamped boundary condition technique suggested by Huang & Sloan (1993) and implemented in Weideman & Reddy (2000). The problem with spurious eigenvalues discussed in Bewley & Liu (1998) is thereby avoided in an effective manner. The integration weights $W(y_j)$ for the Chebyshev grid with the Gauss–Lobatto collocation points were computed using the algorithm from Hanifi, Schmid & Henningson (1996). These weights provide spectral accuracy in the numerical integrations used to assemble the energy measure matrix $\boldsymbol{Q}$. The algebraic Riccati equations found by discretization of (2.5) and (2.12) were solved using the algorithm from Skelton (1988, p. 350); the heart of this algorithm is the solution of the eigenvectors of a $2N \times 2N$ matrix. This

https://doi.org/10.1017/S0022112003003823 Published online by Cambridge University Press

eigenvalue problem was solved via a Schur decomposition technique. Other methods for solving Riccati equations are discussed in e.g. Laub (1991), but were not found to be necessary in the present problem. The kernel computations were performed using Matlab on a 833MHz DEC Alpha workstation and took about 2–3 hours for the kernels presented here.

2.3. *Localized convolution kernels*

2.3.1. *Kernel structure*

The convolution kernels computed using the approach described above are depicted in figures 4 and 5. The control convolution kernels shown in figure 4 angle away from the wall in the *upstream* direction. Considering the shape of the mean flow profile indicated in figure 1, this accounts for the convective delay which requires us to anticipate flow perturbations on the interior of the domain with actuation on the wall somewhere downstream. The estimation convolution kernels shown in figure 5, on the other hand, extend well *downstream* of the measurement point. This accounts for the delay between the motions of the convecting flow structures on the interior of the domain and the eventual influence of these motions on the local drag profile on the wall; during this time delay, the flow structures responsible for these motions convect downstream. Note that the upstream bias of the control kernels and the downstream bias of the estimation kernels, though physically tenable, were not prescribed in the problem formulation. *A posteriori* study of the streamwise, spanwise and wall-normal extent, the symmetry, and the detailed shape of such control and estimation kernels provides us with a powerful new tool with which the fundamental physics of this distributed fluid-mechanical system may be characterized.

2.3.2. *Exponential decay*

As mentioned previously, the present kernels decay exponentially far from the origin. This characteristic was predicted theoretically by Bamieh *et al.* (2002) for a broad class of spatially homogeneous systems. To the best of our knowledge, the present paper presents the first numerical calculation of control and estimation kernels with this property to be derived from the Navier–Stokes equation. In order to better illustrate this decay, control kernels for the normal velocity have been computed for $Re_{\mathfrak{C}} = 2000$ and $\ell = 1$ with high resolution for four different sizes of the computational box. The squared value of the kernels is first integrated in the y-direction to obtain a representation of the kernel weights in the (x, z)-plane. This planar representation is then integrated in z to show the behaviour as a function of x, and integrated in x to show the behaviour as a function of z, as shown in figure 6. The results are normalized by their maximum value. Due to the imposed periodicity, the exponential decay of the kernels is interrupted for small box sizes. However, by increasing the size of the computational box, we clearly see that the decay of the magnitude of the tails is significantly extended, while the shape of the kernel in the vicinity of the origin remains unchanged. In a sufficiently large box, we should see decay of the kernel magnitude over several orders of magnitude as we move away from the origin. However, computation of the kernel over such a large domain is difficult, as it is computationally expensive. Plots such as figure 6 are sufficient to illustrate that the kernels we seek are converged in the region of interest near the origin. The exponential decay depicted in figure 6 is representative of the other kernels computed; similar decay was observed for the v and ω components of the system, for the control and estimation problems, and for the range of values of α and ℓ tested.

https://doi.org/10.1017/S0022112003003823 Published online by Cambridge University Press

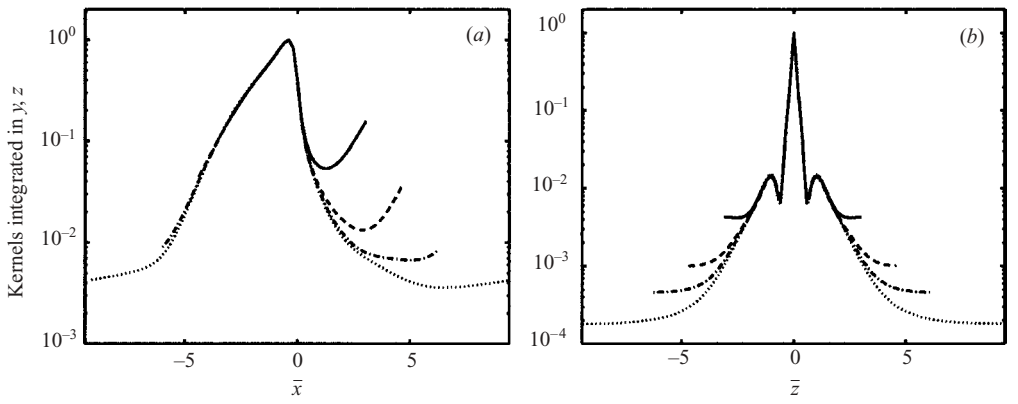


FIGURE 6. Illustration of exponential decay of the control convolution kernel for normal velocity: (*a*) as a function of x, (*b*) as a function of z. Kernels computed with: ———, box size $2\pi \times 2\pi$ with resolution 32×64 in $x \times z$; – – – –, box size $3\pi \times 3\pi$ with resolution 48×96 in $x \times z$; —·—, box size $4\pi \times 4\pi$ with resolution 64×128 in $x \times z$; and ·····, box size $6\pi \times 6\pi$ with resolution 96×192 in $x \times z$. In all cases $\ell = 1$, $Re_{\ell} = 2000$, and the number of gridpoints in y was 70.

3. Simulations

3.1. *Simulation of the nonlinear system*

The direct numerical simulation code of Bewley *et al.* (2001) was used to perform simulations of the constant-mass-flux channel flow system. This code is pseudospectral with 3/2 dealiasing in the streamwise and spanwise directions, and uses an energy-conserving second-order finite-difference technique in the wall-normal direction. Time advancement is performed with the hybrid second-order Crank–Nicholson/third-order Runge–Kutta method developed by Aksevoll & Moin (1995). In this scheme, the treatment of the derivatives in the wall-normal direction is implicit to enhance the stability of the code when blowing/suction boundary conditions are applied. A fractional-step method is used to update the pressure and to enforce the divergence-free constraint. The transition thresholds calculated in Reddy *et al.* (1998) for the uncontrolled system were verified accurately with the present DNS code using initial conditions of precisely the same structure.

To make comparisons easier, the thresholds obtained by Reddy *et al.* (1998) are tabulated in table 1. The initial conditions used for the cases of oblique waves and streamwise vortices are such that they have the 'worst-case' structure in the y-direction that maximizes their transient energy growth. These initial flow perturbations are contained in the lowest wavenumbers represented in the computational box used for the simulations. In addition, random noise in the form of Stokes modes with 1% of the energy of the primary perturbation is added, distributed over all combinations of the wavenumbers $k_x = (0, \pm 1, \pm 2)\, k_{x0}$ and $k_z = (0, \pm 1, \pm 2) k_{z0}$. In the random noise case all the energy is distributed over these wavenumbers. The box size in the streamwise vortex case is $2\pi \times 2 \times \pi$ in $x \times y \times z$ with the fundamental wavenumbers $k_{x0} = 1$ and $k_{z0} = 2$. For both the oblique wave and random noise cases the box size is $2\pi \times 2 \times 2\pi$ in $x \times y \times z$ having the fundamental wavenumbers $k_{x0} = 1$ and $k_{z0} = 1$. The threshold values were found by a bisection algorithm, and were verified using a different resolution. This requires many simulations; a condensed presentation of the

https://doi.org/10.1017/S0022112003003823 Published online by Cambridge University Press

Scenario	$Re_{\mathfrak{L}}$	Resolution	Threshold energy
SV	2000	$16 \times 81 \times 64$	6.48×10^{-6}
	3000	$16 \times 81 \times 64$	1.49×10^{-6}
	5000	$16 \times 81 \times 64$	2.60×10^{-7}
OW	2000	$16 \times 81 \times 64$	2.38×10^{-6}
	3000	$16 \times 81 \times 64$	5.28×10^{-7}
	5000	$16 \times 81 \times 64$	1.16×10^{-7}
N	2000	$32 \times 81 \times 64$	7.25×10^{-5}
	3000	$32 \times 81 \times 64$	2.63×10^{-5}
	5000	$40 \times 97 \times 80$	8.62×10^{-6}

TABLE 1. Uncontrolled transition threshold energy for streamwise vortices (SV), oblique waves (OW) and random noise (N) determined by Reddy *et al.* using a Fourier, Chebyshev, Fourier discretization. The maximum uncertainty in the thresholds shown is $\pm 2.5\%$; that is, initial perturbations with 2.5% more energy cause transition to turbulence, whereas initial perturbations with 2.5% less energy relaminarize.

Scenario	$Re_{\mathfrak{L}}$	Resolution	Threshold energy	Improvement factor
SV	2000	$16 \times 128 \times 64$	6.53×10^{-5}	10
	3000	$16 \times 128 \times 64$	1.44×10^{-5}	9.6
	5000	$16 \times 128 \times 64$	3.00×10^{-6}	11.5
OW	2000	$16 \times 128 \times 64$	2.44×10^{-4}	102
	3000	$16 \times 128 \times 64$	5.77×10^{-5}	109
	5000	$16 \times 128 \times 64$	1.43×10^{-5}	122
N	2000	$32 \times 128 \times 64$	5.08×10^{-4}	7
	3000	$32 \times 128 \times 64$	1.79×10^{-4}	6.8
	5000	$32 \times 128 \times 64$	4.88×10^{-5}	5.7

TABLE 2. Full-state feedback: controlled transition thresholds using a Fourier, finite difference, Fourier discretization. Verified using lower resolution $12 \times 128 \times 42$ and $28 \times 128 \times 58$. The maximum uncertainty in the thresholds shown is $\pm 2\%$. For comparison the energy density of the laminar mean flow is 0.2667 in all cases.

results such as that shown in tables 1 and 2 has required many hundreds of hours of supercomputer time.

3.2. *Modification of transition thresholds with full-state feedback*

Direct numerical simulations of the fully nonlinear Navier–Stokes equations with linear feedback control were performed at three different subcritical Reynolds numbers, $Re_{\mathfrak{L}} = 2000$, 3000 and 5000. Control kernels were computed using the same resolution and box size as in the simulations with $\ell = 0.1$ in all cases. Through an iterative procedure the transition thresholds have been determined for the three different initial flow perturbations (streamwise vortices, oblique waves, and random noise), as reported in table 2 and figure 7. The 'Improvement factor' column in table 2 shows the relation between the threshold for the controlled and uncontrolled cases. If this factor is 2, it means that the initial energy density threshold value is approximately two times higher in the controlled case than in the uncontrolled case. The transition threshold for the streamwise vortex perturbation is increased up to 11.5 times the uncontrolled value, corresponding to more than a threefold increase

https://doi.org/10.1017/S0022112003003823 Published online by Cambridge University Press

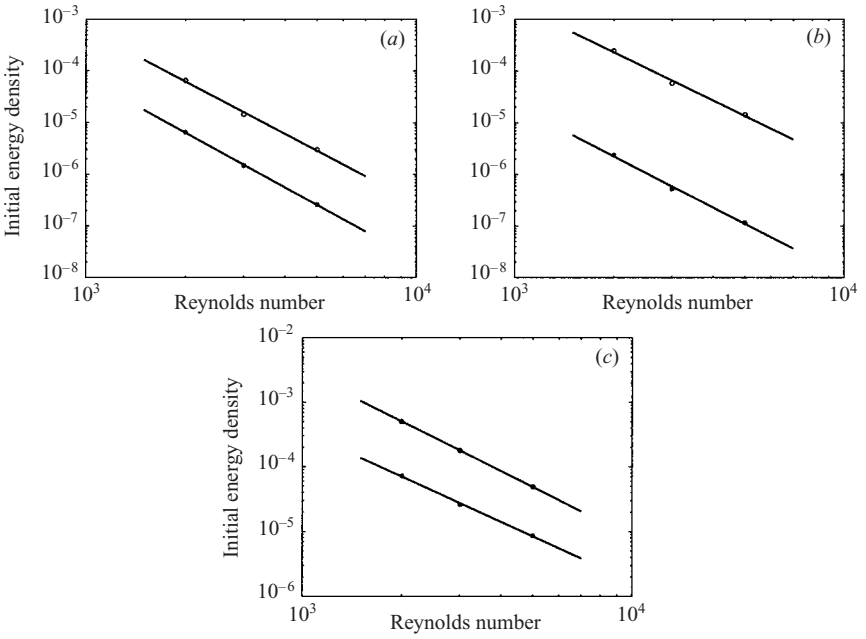


FIGURE 7. Transition threshold energy versus Reynolds number for feedback-controlled plane Poiseuille flow. Shown are the curves obtained from direct numerical simulations with control compared with the uncontrolled cases. One plot for each case starting with various initial conditions: (*a*) optimal streamwise vortices, (*b*) a pair of optimal oblique waves, and (*c*) divergence-free low-wavenumber noise. The open circles are the values obtained with full information state feedback control and the filled circles are the values for the uncontrolled case computed by Reddy *et al.* (1998). The solid lines are least square fits to the data.

in perturbation amplitude. Oblique-wave perturbations, which in the uncontrolled case have the lowest threshold energy, appear to be the easiest to control, since the threshold energy is increased up to 122 times the uncontrolled value. One reason for this might be that the control of the linear growth of the oblique waves efficiently prevents the nonlinear generation of streamwise vortices, which in turn effectively mitigates the generation of streamwise streaks. In the controlled case, the streamwise vortex perturbations have the lowest values of the transition thresholds, suggesting that the underlying transition mechanism in the streamwise vortex scenario is the most powerful one in the controlled flow. The smallest factor for the increase in transition threshold is obtained for the random perturbation; however, even in the controlled system, the threshold energy for transition due to randomly distributed perturbations is uniformly larger (by at least a factor of two) than the other transition scenarios studied. Note that once the flow has transitioned to turbulence, the controller is not able to relaminarize the turbulent flow using the present formulation.

3.3. *Effectiveness of truncated kernels*

Performing truncation of the exponentially decaying tails of the kernels by setting their values to zero beyond a certain radius from the origin (smaller than the box size in which they were computed) results in kernels with spatially compact support. To test the effectiveness of a truncated kernel, the kernel used for the threshold computations was truncated by setting it to zero outside a box with the limits $\bar{x} \in (-3, 1)$ and $\bar{z} \in (-2.5, 2.5)$ using a smoothed step function. Compare

https://doi.org/10.1017/S0022112003003823 Published online by Cambridge University Press

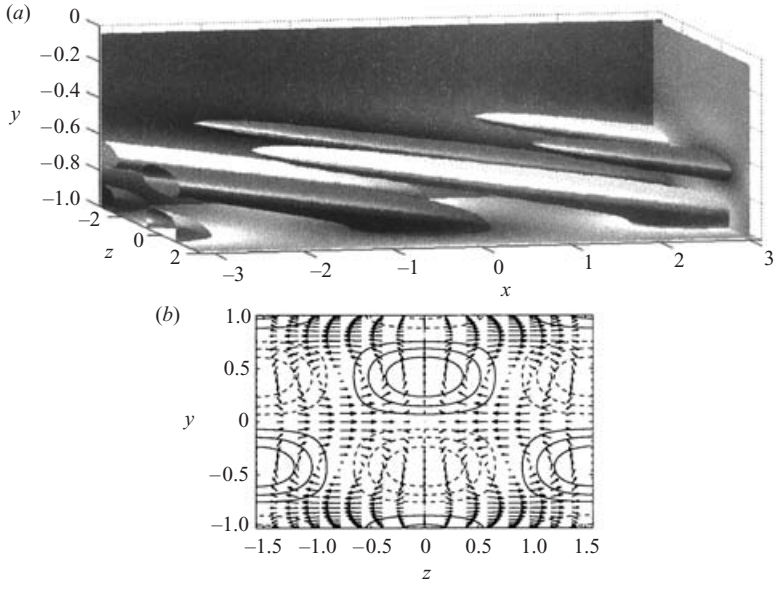


FIGURE 8. Visualizations showing the reaction of the control to the initial conditions depicted in figure 2: (*a*) controlled oblique waves, showing positive (light) and negative (dark) isosurfaces of half of the maximum magnitude of the normal velocity. (*b*) Controlled streamwise vortices, showing contours of v (solid contours for positive velocity and dashed for negative), and cross-flow velocity vectors (projected onto the z, y-plane) at $x = 0$.

with figure 6 to see approximately how much of the kernel information is ignored through this operation. This method of truncation might seem rather abrupt, but more sophisticated schemes for performing the truncation were not found to be necessary. Applying such a truncated kernel in the direct numerical simulation of a random noise perturbation at $Re_{\mathfrak{C}} = 2000$ reproduced the same estimate of the approximate threshold value as for the untruncated kernels reported in table 2 (that is, $5.08 \times 10^{-4} \pm 2\%$). This effectively demonstrates (as expected) that kernel truncation, if performed sufficiently far from the origin, does not significantly degrade the performance of the control, despite the significant reduction in the kernel extent resulting from the truncation and the significant reduction in the computational effort required to implement the feedback calculation when such a calculation is performed as a physical-space convolution.

3.4. *Dynamics of the controlled flows*

In order to try to understand how the controller acts, the oblique wave and streamwise vortex cases with control are now examined in greater detail. In figure 8, the velocity fields, a short time after the full information control is applied, are shown for the oblique wave (*a*) and streamwise vortex (*b*). The action of the control has been studied with the help of animations in order to understand how the control acts on the perturbations.† In the oblique wave case the isosurfaces in figure 8(*a*) are elongated in the streamwise direction, compare with figure 2(*a*), and move down to the wall where they shrink again. New, almost stationary, oblique waves are formed in the centre of the channel and these are then controlled in an out-of-phase fashion

† These animations are available at http://turbulence.ucsd.edu/gallery/transition.

https://doi.org/10.1017/S0022112003003823 Published online by Cambridge University Press

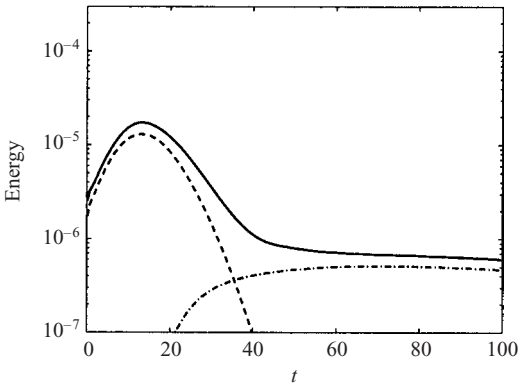


FIGURE 9. Energy evolution in different modes for control of oblique waves. The Reynolds number is $Re_{\xi} = 2000$ and the perturbation energy density is 2.6×10^{-6}. The $(0, 2)$ mode slowly decays to zero after $t = 100$. Plotted are: ———, the total flow perturbation energy in all wavenumber components other than $\{0, 0\}$, as well as the energy in the $\{1, 1\}$ component (– – – –), the $\{0, 2\}$ component (—·—) and the other components (·····). Compare with figure 3(a) for the uncontrolled case.

while accelerating. There is then a rapid reduction of the perturbation amplitude and only a streaky perturbation remains. Even with the help of animations it is difficult to explain the action of the control in detail. The process is complicated and in certain respects non-intuitive, and the advantage of using control theory, which does not require *a priori* understanding of the 'dominant mechanisms' of the transition process, is readily apparent. It is clear that the growth of the oblique wave is efficiently lowered by the control by comparing figure 9 and figure 3(a). It is interesting to note that the control energy is shifted from one set of wavenumbers to another set of wavenumbers as the flow evolves in time, as shown in figure 10. Initially the oblique wave mode is the focus of the control effort, but when this mode has decayed to a level lower than the streak modes, the control focuses its effort on the streak modes instead. It should be noted that the contour levels are not the same in the different frames in figure 10. The largest energy is used initially before the oblique wave mode has its maximum and then it rapidly decays. Thereby the streaks are not forced as efficiently by the oblique waves and the streak amplitude is much lower than in the case without control. When the oblique waves have decayed a streaky structure appears and then the control acts in a way similar to the streamwise vortex case.

In the streamwise vortex case, the wall-normal velocity appears to be approximately of 'opposition' type initially. Figure 8(b) shows the reaction of the control to the streamwise vortex initial condition. In the animation, one can see that the vortices are pushed away from the wall by buffer vortices created by the blowing and suction; a similar result is shown in figure 12(c) of Bewley & Liu (1998). In addition, *virtual walls* (using the terminology of Hammond, Bewley & Moin 1998) are created near the centre of the channel. Streamwise streaks rapidly develop in the regions between the real walls and the virtual walls as a result of the blowing and suction applied. The virtual walls then move slowly towards the real walls as the blowing and suction decrease, and the vortices reappear between the virtual walls in the centre of the channel. The streaks in the near-wall region decay as the blowing and suction weaken, and since a low-speed streak is located where the vortices in the centre of the channel move momentum from the inner part of the channel towards the virtual wall, a high-speed

https://doi.org/10.1017/S0022112003003823 Published online by Cambridge University Press

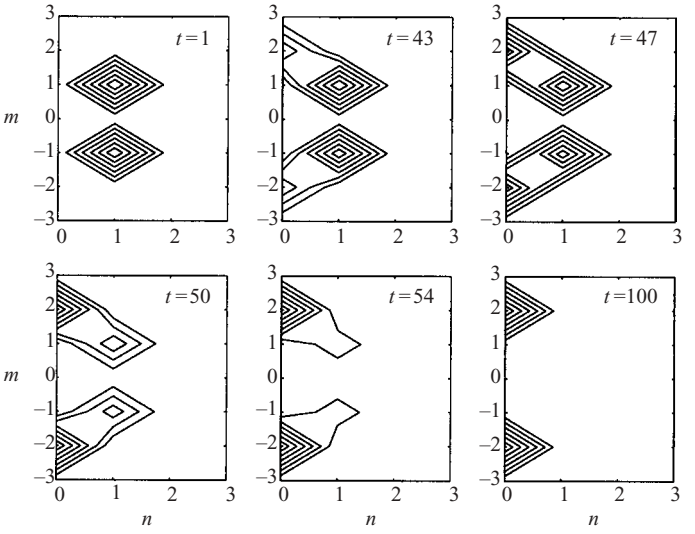


FIGURE 10. Contour plot of $\phi^2(k_x, k_z)$ for control of oblique waves at $t = [1, 43, 47, 50, 54, 100]$. where $k_x = n\,k_{x0}$ and $k_z = m\,k_{z0}$. Notice that the contour levels are not equal in the different plots but decreases with time and the maximum level is $[9.37 \times 10^{-7},\ 4.25 \times 10^{-9},\ 2.56 \times 10^{-9},\ 2.49 \times 10^{-9},\ 2.47 \times 10^{-9},\ 1.18 \times 10^{-9}]$ for each frame respectively.

streak is created above the low-speed streak (and vice versa). These streaks in the interior of the channel merge slowly, through diffusion, then slowly decay. The virtual walls slowly move towards the centre of the channel again as the streaks decrease and eventually disappear.

3.5. *Convergence of estimator with feedback from measurements*

Estimating the state of the flow from available measurements is a crucial step towards practical implementation of this type of controller. Possible measurements are e.g. the components of the shear stress and pressure fluctuations on the wall. Many different independent measurements give more information about the state of the flow. In the present study we have focused on the use of a measurement of the wall-normal derivative of the wall-normal vorticity component (note that this quantity is easily calculated from measurements of $\partial u/\partial y$ and $\partial w/\partial y$). Using this one measurement quantity appears to be sufficient to get exponential convergence of the state estimate, but it is rather slow. The estimator forcing kernels are computed as described in § 2.1.2 with $\alpha = 0.1$, and then used to force the flow in a fully nonlinear simulation. This is known as an *extended* Kalman filter. Estimation of a nonlinear fluid system using linear estimator feedback is discussed further in Bewley (1999). The initial state in the estimator is an unperturbed laminar flow at the same Reynolds number as the measured flow in all cases presented here. In figure 11 the energy of the difference between the state in the measured flow and in the estimator is plotted versus time. The initial state in the unknown flow is a random perturbation at an energy level below the transition threshold. The initial guess in the estimator is an unperturbed laminar flow at $Re_{\bar{q}} = 3000$. Estimator forcing kernels are computed for both $\boldsymbol{G}_1\boldsymbol{G}_1^* = \boldsymbol{Q}$ and $\boldsymbol{G}_1\boldsymbol{G}_1^* = \boldsymbol{I}$. Using either estimator, there is an initial transient increase in the error after which it decays at an exponential rate. The transient is due to the fact that it is not possible to obtain uniform decay of the state error using only the current measurements, as the system representing the estimator error is non-normal,

https://doi.org/10.1017/S0022112003003823 Published online by Cambridge University Press

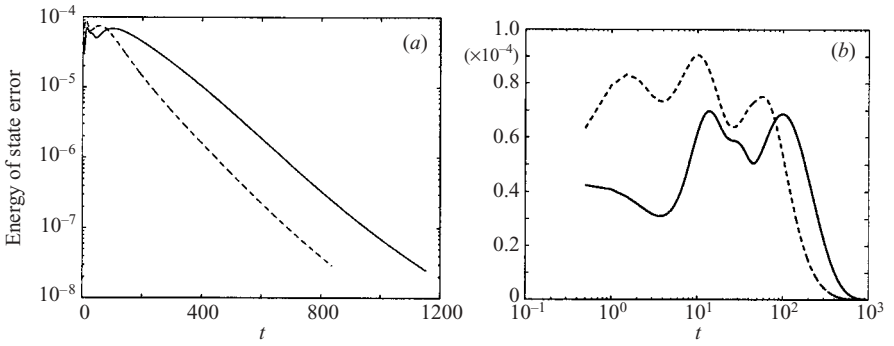


FIGURE 11. Convergence of estimator computed with $\alpha = 0.1$ for a random perturbation with an energy just below the transition threshold at $Re_{\zeta} = 3000$. Solid line with $\boldsymbol{G}_1\boldsymbol{G}_1^* = \boldsymbol{Q}$ and dashed line with $\boldsymbol{G}_1\boldsymbol{G}_1^* = \boldsymbol{I}$. (*a*) Logarithmic in vertical axis, (*b*) logarithmic in horizontal axis.

just like the controlled closed-loop system. For more discussion about the closed-loop properties of the linear system see Bewley & Liu (1998). Using $\boldsymbol{G}_1\boldsymbol{G}_1^* = \boldsymbol{Q}$ gives a small transient during a long time whereas using $\boldsymbol{G}_1\boldsymbol{G}_1^* = \boldsymbol{I}$ gives a larger transient for a shorter time. Since both the initial behaviour and the convergence are important issues, there is no clear reason why one would be preferred to the other. The amplitude of the initial transient could be of importance when the perturbation energies are large and nonlinear effects are strong. If the estimator state undergoes transition due to this transient, the compensator cannot be expected to work particularly well. For this reason the estimator with $\boldsymbol{G}_1\boldsymbol{G}_1^* = \boldsymbol{Q}$ that has a lower amplitude of the transient is the primary choice for the estimator-based control studies that follow.

3.6. *Modification of transition thresholds with estimator-based control*

In the case of measurement-based control we run two different nonlinear direct numerical simulations simultaneously: one with the initial perturbation we wish to control (this represents our 'physical system' in this test), and one with measurement feedback and no initial perturbation (this represents our 'estimator' in this test). Measurements are taken in both simulations and the difference between the two is used to force the estimator using the estimator feedback kernels. The state in the estimator, which as shown in the previous section for the uncontrolled case converges exponentially to the correct state, is then used to compute the feedback control which is then applied in both simulations simultaneously. This combination of estimator and controller is called a measurement-based dynamic compensator. The control kernels are the same as used for the full information case and the estimation kernels are computed with the same box size and resolution as the simulations with $\alpha = 0.1$.

The compensator was first tested for an oblique wave at $Re_{\zeta} = 2000$, and a comparison of the perturbation energy with the full information controller and for the uncontrolled flow is plotted in figure 12. In this case the initial energy density was 1.25×10^{-5}, but the perturbation did not have the optimal shape in y and no additional random noise was added. The total energy reduction for the full-information controller and the measurement-based compensator appears to be of the same order. The compensator performance was even closer to that of the full information controller if a good initial guess for the state in the estimator was provided. This demonstrates that the compensator is successful in reducing the energy growth of an oblique wave perturbation, but the question remains as to what happens

https://doi.org/10.1017/S0022112003003823 Published online by Cambridge University Press

Scenario	$Re_{\mathcal{L}}$	Resolution	Threshold energy	Improvement factor
SV	2000	$16 \times 128 \times 64$	1.88×10^{-5}	2.9
OW	2000	$16 \times 128 \times 64$	1.38×10^{-5}	5.8
N	2000	$16 \times 128 \times 64$	9.50×10^{-5}	1.31
	3000	$16 \times 128 \times 32$	3.38×10^{-5}	1.28
	5000	$16 \times 128 \times 32$	1.13×10^{-5}	1.30

TABLE 3. Compensator-controlled transition thresholds using a Fourier, finite difference, Fourier discretization, taking $\boldsymbol{G}_1\boldsymbol{G}_1^* = \boldsymbol{Q}$, for the initial perturbations: SV: streamwise vortex, OW: oblique wave and N: random perturbation. The maximum uncertainty in the thresholds shown is $\pm 6\%$. For comparison the energy density of the laminar mean flow is 0.2667 in all cases.

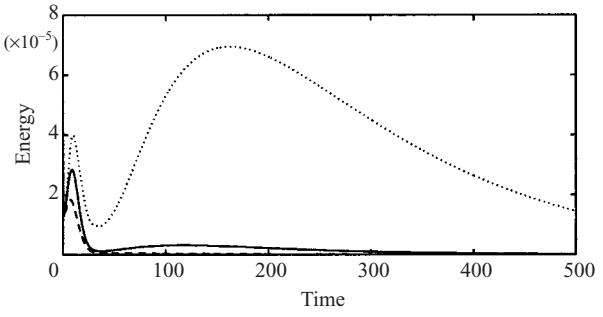


FIGURE 12. Performance of full-information linear controller (dashed) and compensator using $\boldsymbol{G}_1\boldsymbol{G}_1^* = \boldsymbol{Q}$ (solid) compared to the uncontrolled (dotted) energy evolution.

when the amplitude of the perturbations is large and noise is present. In order to test the compensator performance, the 'worst-case' situation when the initial state in the estimator is an unperturbed flow is considered.

Simulations are performed at Reynolds number 2000 for all three types of initial perturbations; table 3 contains the resulting transition thresholds from these simulations. With $\boldsymbol{G}_1\boldsymbol{G}_1^* = \boldsymbol{I}$, only one case at $Re_{\mathcal{L}} = 2000$ with random noise is considered. The transition threshold for the streamwise vortex perturbation is increased by 2.9 times the uncontrolled value. Oblique-wave perturbations appear to be the easiest to control using the compensator (as with the full-state feedback controller), and the threshold energy is increased by 5.8 times the uncontrolled value. In the compensator-controlled case the oblique-wave perturbations, as opposed to streamwise vortices in the full information control cases, have the lowest values of the transition threshold.

As for the full-information case, the smallest factor for the increase in transition threshold is obtained for the random perturbation and is only 1.3, but again the threshold energy in the random perturbation cases is much larger than in the other two cases, so the control effectiveness in this case is probably not as important as the control effectiveness in the other two cases. For estimator feedback computed with $\boldsymbol{G}_1\boldsymbol{G}_1^* = \boldsymbol{I}$ (not shown in table 3) in the $Re_{\mathcal{L}} = 2000$ random-noise case (N), the initial transient in the estimator is larger, but the improvement factor is increased to 1.48 with the corresponding compensator. The large initial transient in the estimator in this

https://doi.org/10.1017/S0022112003003823 Published online by Cambridge University Press

case therefore does not seem to be the dominant factor in the overall performance. The choice of $\boldsymbol{G}_1$ is a delicate issue, and further research is needed to find the optimal choice for transition control. Remember also that the results can be improved by providing a good initial guess in the estimator, suggesting an alternative route to improved performance. The small increase in threshold values for the random noise perturbation in the compensator case further suggests that this is the most difficult perturbation to control. For the random noise perturbation, simulations at the higher Reynolds numbers 3000 and 5000 are performed to verify that the factor is kept approximately constant in the compensator case also, as seen in table 3.

4. Discussion

The effectiveness of the strategy for control and estimation of transitional flows presented in § 2 has been quantified for three significant types of perturbations in subcritical channel flow studied in Reddy *et al.* (1998). A large number of direct numerical simulations have been performed in order to determine the transition threshold energies for the controlled flows both in the full-information and measurement-based settings. The localization of the kernels with exponentially decaying tails and the small effect on their efficiency from truncation compared to the untruncated kernels has been demonstrated.

In the full-information control case, we have shown that the controller can increase the threshold energies for transition by as much as 122 times the uncontrolled value for oblique-wave perturbations and approximately 10 and 7 times for the streamwise-vortex and random-noise perturbations respectively. The lowest threshold value is obtained for the streamwise vortices in the controlled case, indicating that the transition mechanism involved in this scenario is the most powerful one. The factor of increase in the threshold energies is approximately constant for different Reynolds numbers for all types of perturbations considered. This results in lower threshold values for higher Reynolds numbers.

The measurement-based state estimator was implemented as an extended Kalman filter and shown to give exponential convergence of the estimated state to the measured state. This convergence was found to be rather slow, and further research is necessary in order to improve the results. Additional measurements, such as wall pressure fluctuations and independent streamwise and spanwise skin friction measurements, should be implemented in an attempt to accelerate convergence.

The full compensator performed well for the early stages of oblique transition. For the transition threshold calculations we have not quantified the compensator performance to the same extent as in the full-information case. One reason for this is that these simulations are twice as costly compared to the full-information case since two flow fields have to be marched in time simultaneously. As noted earlier the estimator convergence also needs to be improved. A rule of thumb when designing compensators is that the estimator should converge faster than the controller in order to achieve good and robust performance. The development of more efficient estimators will hopefully provide a means to raise these threshold values for the compensator to levels close to those obtained with the full-information controller.

Since the problem we are studying in this paper is idealized, it should be clarified how these results will lead to practical feedback compensators to be used in engineering applications. The advantage of the current approach is that truncation in physical space results in kernels that have compact spatial support with maintained performance, and this facilitates a convenient strategy for decentralized physical-space

https://doi.org/10.1017/S0022112003003823 Published online by Cambridge University Press

implementation. For a thorough discussion about the implications of this property of the kernels and practical implementation issues the reader is deferred to Bewley (2001).

4.1. *Extensions*

4.1.1. $\mathscr{H}_\infty$ *control*

The present formulation can, with small modifications, also be used to compute robust ($\mathscr{H}_\infty$) compensators. The idea of robust control provides a very natural means of focusing the compensation to respond appropriately to disturbance forcing of worst-case structure. It is well known in the controls literature that optimal (H_2) controllers typically do quite well when full-state information is available, but the benefits of designing robust ($\mathscr{H}_\infty$) compensator feedback to respond to worst-case system disturbances can sometimes be quite significant when only limited noisy measurements are available. The idea of designing controls to mitigate the worst-case system response is especially important when one is attempting to prevent the triggering of hydrodynamic transition by such worst-case disturbances. In the case of $\mathscr{H}_\infty$ control, the problems of control and estimation are coupled, and the separation principle no longer applies. The general framework for linear robust control is described in detail in Doyle *et al.* (1989). In Bewley & Liu (1998), $\mathscr{H}_\infty$ compensation was calculated for one wavenumber pair of the present problem, and was shown to provide a significantly better response to worst-case perturbations in the linear setting than optimal $\mathscr{H}_2$ compensation. A similar study was also performed by Baramov *et al.* (2000).

4.1.2. *Spatially developing flows*

The extension to spatially evolving flows is straightforward. The modification necessary is to include the base flow from Blasius, Falkner–Skan, or Falkner–Skan–Cooke flows and then proceed as described in the present paper to compute the control and estimation kernels. Assuming that the flow is locally parallel, a number of kernels computed using the Orr–Sommerfeld/Squire equations with the local mean flow profiles can then be applied at different streamwise positions to cover a large control domain. This is done using one control kernel in one streamwise interval in Högberg & Henningson (2002) for stationary as well as time-varying perturbations. Application of measurement-based control in this case is a natural next step.

4.1.3. *Reduced-order compensation*

The current system has very large dimensions and could be difficult to realize in real-time applications. One solution to this problem is to perform model reduction of the system and then develop a low-dimensional compensator. Open-loop model reduction for control of transition in two-dimensional channel flow is evaluated in e.g. Cortelezzi & Speyer (1998) and Joshi *et al.* (1999), and the three-dimensional problem is discussed in Kang *et al.* (1999). This is an active area of research and many possibilities remain to explored.

The authors thank Bassam Bamieh and Scott Miller for useful discussions related to this work, and Satish Reddy for providing the initial conditions for the transition simulations.

REFERENCES

Abergel, F. & Temam, R. 1990 On some control problems in fluid mechanics. *Theor. Comput. Fluid Dyn.* **1**, 303–325.

https://doi.org/10.1017/S0022112003003823 Published online by Cambridge University Press

Aksevoll, K. & Moin, P. 1995 Large eddy simulation of turbulent confined co-annular jets and turbulent flow over a backward facing step. *Rep.* TF-63. Thermosciences Division, Dept. of Mech. Engng, Stanford University.

Bamieh, B., Paganini, F. & Dahleh, M. 1998 Optimal control of distributed actuator and sensor arrays. *Proc. SPIE – The Int. Soc. for Optical Engng* **3323**, 467–478.

Bamieh, B., Paganini, F. & Dahleh, M. 1999 Optimal control of distributed arrays with spatial invariance. In *Lecture Notes in Control and Information Sciences*, vol. 245 (ed. A. Garullie, A. Tesi & A. Vicino) Springer.

Bamieh, B., Paganini, F. & Dahleh, M. 2002 Distributed control of spatially-invariant systems. *IEEE Trans. Automat. Contr.* **47**, 1091–1107.

Baramov, L., Tutty, O. R. & Rogers, E. 2000 Robust control of plane Poiseuille flow. *AIAA Paper* 2000-2684.

Bewley, T. R. 1999 Linear control and estimation of nonlinear chaotic convection: harnessing the butterfly effect. *Phys. Fluids* **11**, 1169–1186.

Bewley, T. R. 2001 Flow control: new challenges for a new Renaissance *Prog. Aerospace Sci.* **37**, 21–58.

Bewley, T. R. & Liu, S. 1998 Optimal and robust control and estimation of linear paths to transition. *J. Fluid Mech.* **365**, 305–349.

Bewley, T. R. & Moin, P. 1994 Optimal control of turbulent channel flow for reduction of pressure fluctuations. In *Active Control of Vibration and Noise* (ed. K. W. Wang *et al.*) ASME.

Bewley, T. R., Moin, P. & Temam, R. 2001 DNS-based predictive control of turbulence: an optimal benchmark for feedback algorithms. *J. Fluid Mech.* **477**, 179–225.

Butler, K. M. & Farrell, B. F. 1992 Three-dimensional optimal perturbations in viscous shear flows. *Phys. Fluids* A **4**, 1637–1650.

Carlson, D. R., Widnall, S. E. & Peeters, M. F. 1982 A flow visualization study of transition in plane Poiseuille flow. *J. Fluid Mech.* **121**, 487–505.

Choi, H., Moin, P. & Kim, J. 1994 Active turbulence control for drag reduction in wall-bounded flows. *J. Fluid Mech.* **262**, 75–110.

Choi, H., Temam, R., Moin, P. & Kim, J. 1993 Feedback control for unsteady flow and its application to the stochastic Burgers equation. *J. Fluid Mech.* **253**, 509–543.

Collis, S. S., Chang, Y., Kellog, S. & Prabhu, R. D. 2000 Large eddy simulation and turbulence control *AIAA Paper* 2000-2564.

Cortelezzi, L. & Speyer, J. L. 1998 Robust reduced-order controller of laminar boundary layer transitions. *Phys. Rev.* E **58**, 1906–1910.

Cortelezzi, L., Speyer, J. L., Lee, K. H. & Kim, J. 1998 Robust reduced-order control of turbulent channel flows via distributed sensors and actuators. *Proc. 37th IEEE Conf. on Decision and Control*, vol. 2, pp. 1906–1911.

Doyle, J. C., Glover, K., Khargonekar, P. P. & Francis, B. A. 1989 State-space solutions to standard $\mathscr{H}_2$ and $\mathscr{H}_\infty$ control problems. *IEEE Trans. Automat. Contr.* **34**, 831–847.

Drazin, P. G. & Reid, W. H. 1981 *Hydrodynamic Stability*. Cambridge University Press.

Farrell, B. F. & Ioannou, P. J. 1996 Turbulence suppression by active control. *Phys. Fluids* **8**, 1257–1268.

Gad-el-Hak, M. 1996 Modern developments in flow control. *Appl. Mech. Rev.* **49**, 364–379.

Hammond, E. P., Bewley, T. R. & Moin, P. 1998 Observed mechanisms for turbulence attenuation and enhancement in opposition-controlled wall-bounded flows. *Phys. Fluids* **10**, 2421–2423

Hanifi, A., Schmid, P. J. & Henningson D. S. 1996 Transient growth in compressible boundary layer flow. *Phys. Fluids* **8**, 826–836.

Henningson, D. S. 1996 Comment on "Transition in shear flows. Nonlinear normality versus non-normal linearity" [Phys. Fluids 7, 3060 (1995)] *Phys. Fluids* **8**, 2257–2258.

Henningson, D. S. & Reddy, S. C. 1994 On the role of linear mechanisms in transition to turbulence. *Phys. Fluids* **6**, 1396–1398.

Herbert, T. 1988 Secondary instability of boundary layers. *Annu. Rev. Fluid Mech.* **20**, 487–526.

Högberg, M. & Bewley, T. R. 2000 Spatially localized convolution kernels for feedback control of transitional flows. In *Proc. 39th IEEE Conf. on Decision and Control*, vol. 4, pp. 3278–3283.

Högberg, M. & Henningson, D. S. 2002 Linear optimal control applied to instabilities in spatially developing boundary layers. *J. Fluid Mech.* **470**, 151–179.

https://doi.org/10.1017/S0022112003003823 Published online by Cambridge University Press

Hu, H. H. & Bau, H. H. 1994 Feedback control to delay or advance linear loss of stability in planar Poiseuille flow. *Proc. R. Soc. Lond.* A **447**, 299–312.

Huang, W. & Sloan, D. M. 1993 The pseudo-spectral method for solving differential eigenvalue problems. *J. Comput. Phys.* **111**, 399–409.

Ito, K. & Morris, K. A. 1998 An approximation theory of solutions to operator Riccati equations for $\mathscr{H}^\infty$ control. *SIAM J. Control Optim.* **36**, 82–99.

Joshi, S. S., Speyer, J. L. & Kim, J. 1997 A systems theory approach to the feedback stabilization of infinitesimal and finite-amplitude disturbances in plane Poiseuille flow. *J. Fluid Mech.* **332**, 157–184.

Joshi, S. S., Speyer, J. L. & Kim, J. 1999 Finite-dimensional optimal control of Poiseuille flow. *J. Guidance, Control, Dynamics* **22**, 340–348.

Kang, S. M., Ryder, V., Cortelezzi, L. & Speyer, J. L. 1999 State-space formulation and controller design for three-dimensional channel flows *Proc. Am. Control Conf.* **3**, 1627–1631.

Kim, J. & Lim, J. 2000 A linear process in wall-bounded turbulent shear flows *Phys. Fluids* **12**, 1885–1888.

Koumoutsakos, P. 1997 Active control of vortex-wall interactions. *Phys. Fluids* **9**, 3808–3816.

Koumoutsakos, P. 1999 Vorticity flux control for a turbulent channel flow. *Phys. Fluids* **11**, 248–250.

Laub, A. J. 1991 Invariant subspace methods for the numerical solution of Riccati equations. In *The Riccati Equation* (ed. S. Bittanti, A. J. Laub & J. C. Willems), pp. 163–196. Springer.

Lee, C., Kim, J., Babcock, D. & Goodman, R. 1997 Application of neural network to turbulence control for drag reduction. *Phys. Fluids* **9**, 1740–1747.

Lee, C., Kim, J. & Choi, H. 1998 Suboptimal control of turbulent channel flow for drag reduction. *J. Fluid Mech.* **358**, 245–258.

Lee, K. H., Cortelezzi, L., Kim, J. & Speyer, J. L. 2001 Application of robust reduced-order controller to turbulent flows for drag reduction. *Phys. Fluids* **13**, 1321–1330.

Lumely, J. & Blossey, P. 1998 Control of turbulence. *Annu. Rev. Fluid Mech.* **30**, 311–327.

Metcalfe, R. W. 1994 Boundary layer control: A brief review. In *Computational Fluid Dynamics '94, Invited lectures of the Second European CFD Conference; Stuttgart, Germany*. (ed. S. Wagner, J. Periaux & E. Hirschel.), pp. 52–60. John Wiley & Sons.

Orszag, S. A. 1971 Accurate solution of the Orr–Sommerfeld equation. *J. Fluid Mech.* **50**, 689–703.

Paganini, F. & Bamieh, B. 1998 Decentralization properties of optimal distributed controllers. *Proc. 37th IEEE Conf. on Decision and Control, Tampa, FL, 16–18 Dec.* vol. 2, pp. 1877–1882.

Patel, V. C. & Head, R. 1969 Some observations on skin friction and velocity profiles in fully developed pipe and channel flows. *J. Fluid Mech.* **38**, 181–201.

Rebbeck, H. & Choi, K.-S. 2001 Opposition control of near-wall turbulence with a piston type actuator. *Phys. Fluids* **13**, 2142–2145.

Reddy, S. C. & Henningson, D. S. 1993 Energy growth in viscous channel flows. *J. Fluid Mech.* **252**, 209–238.

Reddy, S. C., Schmid, P. J., Baggett, J. S. & Henningson, D. S. 1998 On stability of streamwise streaks and transition thresholds in plane channel flows. *J. Fluid Mech.* **365**, 269–303.

Schmid, P. J. & Henningson, D. S. 2001 *Stability and Transition in Shear Flows*. Springer.

Skelton, R. E. 1988 *Dynamic Systems Control, Linear Systems Analysis and Synthesis*. John Wiley & Sons.

Thomas, A. S. W. 1990 Active wave control of boundary-layer transition. In *Viscous Drag Reduction in Boundary Layers* (ed. D. M. Bushnell & J. N. Hefner). AIAA. *Control, Tampa, FL, 16–18 Dec.* vol. 2, pp. 1877–1882.

Trefethen, L. N., Trefethen, A. E., Reddy, S. C. & Driscoll, T. A. 1993 Hydrodynamic stability without eigenvalues. *Science* **261**, 578–584.

Weideman, J. A. C. & Reddy, S. C. 2000 A Matlab Differentiation Matrix Suite. *ACM Trans. Math. Software* **26**, 465–519

https://doi.org/10.1017/S0022112003003823 Published online by Cambridge University Press